Title

A multimodal approach to revisiting oxidation defects in Cr2O3

Journal

npj Materials Degradation, 6(1)

ISSN

2397-2106

Authors

Auguste, R

Chan, HL

Romanovskaia, E

et al.

Publication Date

2022

DOI

10.1038/s41529-022-00269-7

ARTICLE OPEN

Check for updates

A multimodal approach to revisiting oxidation defects in Cr_2O_3

R. Auguste[1]✉, H. L. Chan[2]✉, E. Romanovskaia[2], J. Qiu[1], R. Schoell[3], M. O. Liedke[4], M. Butterling[4], E. Hirschmann[4], A. G. Attallah[4,5], A. Wagner[4], F. A. Selim[6], D. Kaoumi[3], B. P. Uberuaga[7], P. Hosemann[1,8]✉ and J. R. Scully[2]✉

The oxidation of chromium in air at 700 °C was investigated with a focus on point defect behavior and transport during oxide layer growth. A comprehensive set of characterization techniques targeted characteristics of chromium oxide microstructure and chemical composition analysis. TEM showed that the oxide was thicker with longer oxidation times and that, for the thicker oxides, voids formed at the metal/oxide interface. PAS revealed that the longer the oxidation time, there was an overall reduction in vacancy-type defects, though chromium monovacancies were not found in either case. EIS found that the longer oxidized material was more electrochemically stable and that, while all oxides displayed p-type character, the thicker oxide had an overall lower charge carrier density. Together, the results suggest anion oxygen interstitials and chromium vacancy cluster complexes drive transport in an oxidizing environment at this temperature, providing invaluable insight into the mechanisms that regulate corrosion.

npj Materials Degradation (2022)6:61 ; https://doi.org/10.1038/s41529-022-00269-7

INTRODUCTION

Oxidation and corrosion of metals and alloys has been studied for decades because of their technological importance. Oxidation can occur at different temperatures, altering point defect types and concentrations, which play an important role in corrosion. Chromium, specifically, has been widely studied and implemented because the passivating chromium oxide film formed during oxidation can be highly corrosion resistant[1–4]. Unalloyed chromium is not used as a construction material by itself, but in many cases the primary reason for adding chromium to alloys is precisely the development of a corrosion resistant oxide layer. When a sufficient concentration of Cr is added to iron, nickel, or cobalt based alloys, Cr_2O_3 is formed in a continuous layer on the surface and ion transport is reduced to the point where corrosion of the underlying metal is substantially suppressed. Ion mobility is slower than in Fe_2O_3[5,6]. Point defects play an important role in regulating the effectiveness and establishing the limits of Cr_2O_3 corrosion protection, so significant theoretical, experimental, and modelling efforts have been undertaken to understand the nature of point defects that control oxidation and their diffusion mechanisms[7–23]. Several theoretical efforts have focused on growth kinetics of the oxide layer[7–9]. There is still a large spread in the reported self-diffusion coefficients and defect formation energies from various experimental studies[9–19]. In recent years, some modelling efforts have focused on self-diffusion coefficients in pure Cr, Cr_2O_3, and Cr-containing alloys using density functional theory[20–23]. While each of these approaches provides its own insights on the nature of point defects' charge state, mobility, and formation energies, there have been no efforts to unite the results and insights of a variety of techniques in a single study.

Over the past six decades, a wide variety of experimental techniques has been used to study the scale growth of the oxide and point defect diffusion within the oxide layer. Raman spectroscopy can confirm the chemical and structural nature of the oxide layer, which is expected to be Cr_2O_3, but cannot provide microstructural information. Transmission electron microscopy (TEM) is useful for assessing the oxide's structure, composition, and microstructure (including pores, grains and grain boundaries, and dislocations) within the oxide layer and any interface with the metal. Positron annihilation spectroscopy (PAS) and electrochemical impedance spectroscopy (EIS) probe smaller point defects and their agglomerations. Coupling these experimental methods can shine light on the fundamental mechanism for extended defect formation and stability since each method can sample different properties with different accuracy and confidence.

PAS has been widely used to probe atomic scale defects in solids, such as vacancies, vacancy clusters, dislocations, and nanometer-scale voids[24]. PAS has also been used for probing radiation damage on neutron and ion-beam irradiated materials[25,26]. The variable energy positron beams identify vacancy-type defect density at specific depths by implanting positrons of defined kinetic energy E_p into a solid. The two types of positron spectroscopy used in this manuscript are complementary techniques to evaluate point defects. Doppler broadening variable energy positron annihilation spectroscopy (DB-VEPAS) can provide information about the overall defect density as a function of depth as well as fingerprints of the defects' atomic arrangement. Variable energy positron annihilation lifetime spectroscopy (VEPALS) quantifies vacancy-type defect size and concentration based on positron lifetimes that scale with the local electron density. Hence, analyzing a given oxide layer's defect population during corrosion can be more robustly studied. Previous positron studies investigated the relative defect content of corroded iron alloys containing chromium[27–30] using DB-VEPAS, however the VEPALS

[1]Department of Nuclear Engineering, University of California, Berkeley, Berkeley, CA, USA. [2]Department of Materials Science & Engineering, University of Virginia, Charlottesville, VA, USA. [3]Department of Nuclear Engineering, North Carolina State University, Raleigh, NC, USA. [4]Institute of Radiation Physics, Helmholtz-Zentrum Dresden - Rossendorf, Bautzner Landstraße 400, 01328 Dresden, Germany. [5]Physics Department, Faculty of Science, Minia University, P.O. 61519 Minia, Egypt. [6]Department of Physics and Astronomy, Bowling Green State University, Bowling Green, OH, USA. [7]Materials Science and Technology Division, Los Alamos National Laboratory, Los Alamos, NM, USA. [8]Lawrence Berkeley National Laboratory, Berkeley, CA, USA. ✉email: auguste@berkeley.edu; hc4ry@virginia.edu; peterh@berkeley.edu; jrs8d@virginia.edu

technique can also provide a quantitative assessment of the defect type and size.

Apart from spectroscopic studies based on positron annihilation, AC electrochemical techniques have also been employed to characterize point defects of semiconductors and passivity of structural materials in aqueous media. A popular method is the Mott-Schottky approach, where a high frequency AC sinusoidal voltage is applied over a range of DC potentials to an electrode with a semiconductor oxide in an electrolyte. Then, the measured impedance can be mathematically correlated with the dopant concentration or charge carrier density of ionic defects. This is made possible because the oxide and its space charge region exhibits a dielectric behavior[31]. The method relies on probing the compensating electronic defects that maintain electroneutrality with respect to the ionic defects of interest. The Mott-Schottky approach can therefore determine whether an oxide is p-type or n-type[32]. For example, Wielant et al. utilized electrochemical impedance spectroscopy (EIS) and Mott-Schottky methods and found that the charge carriers within iron thermal oxides (hematite and magnetite) exhibit n-type behavior and their concentration increase with higher N_2 content in the oxidation atmosphere[33]. This technique can help to quantify the correlation between point defect population and characteristics of the corrosion behavior of oxidized metals regulated by diffusive processes. These processes are often observed in DC electrochemistry experiments, e.g. potentiostatic and potentiodynamic polarization techniques of passivated transition metals used in structural applications[34–36].

However, the Mott-Schottky technique is insensitive to a particular ionic crystal point defect identity and does not distinguish between vacancy or interstitials. Using chromium oxide formed in aqueous solution as an example, the Mott-Schottky technique can identify the p-type characteristics and its population[34], but it is impossible to tell whether the predominant point defect type is cation vacancies or anion interstitials as both are charged compensated by holes. Furthermore, the Mott-Schottky approach assumes uniform distribution of ionic defects and does not provide information on the depth dependence of dopant concentrations but rather the effective average property assuming a parallel plate capacitor. This creates a challenge in fully understanding passivity since the different types of point defects and their concentrations dictate the mechanism of atomistic scale transport processes contributing to or controlling corrosion of passivated materials in thick films[35]. For instance, Wagner oxidation processes rely on both ionic diffusivity and electronic conductivity in the development of the classic parabolic rate law[37]. The rate of iron oxidation in these cases is often limited by anion or cation diffusion rates and defect densities. For instance, the diffusion of cations through the ferrite spinel regulates redox processes at the oxide/gas interface.

Despite the plethora of experimental and computational techniques employed to study the properties of chromium oxides as well as other semiconductors, efforts utilizing each technique are parallel but separate, generating a knowledge gap that hinders the progress of oxide research. For example, at the time of writing, it is unclear whether vacancy sensitive PALS can be quantitatively and qualitatively presented against electrochemical methods, such as the Mott-Schottky technique, as well as data predicted from Density Functional Theory calculations.

In this manuscript, the objective is to obtain a comprehensive picture of the overall defect density and microstructure in the oxide layer of thermally oxidized Cr. This work combines oxide microstructure and chemical composition analysis by means of Raman spectroscopy and transmission electron microscopy with point defect evaluation from positron annihilation spectroscopy and electrochemical impedance spectroscopy, thereby corroborating the findings of each technique. The results provide insights on void agglomeration near the metal/oxide interface, decreasing overall defect concentration, and defect transport during the growth of chromium oxide layers.

RESULTS AND DISCUSSION

TEM and Raman spectroscopy

Figures 1 and 2 show the cross-sectional TEM bright field images of the as-polished chromium oxidized at 700 °C in air for 24 h and 5 days, respectively. Selected area electron diffraction (SAED) patterns label both grown oxide layers as Cr_2O_3. As expected, the thickness of the oxide increases with increasing oxidation time. There is a visible oxide film of 55 to 500 nm on chromium oxidized at this temperature for 24 h. The oxide layer does not grow uniformly in thickness across the sample. Increasing the oxidation to 5 days creates an oxide with an average thickness of around 1000 nm. The 5 day Cr oxide also exhibited larger oxide grains towards the outside surface of the sample while showing smaller grains at the oxide/metal interface. Both oxides are polycrystalline of various orientations and feature large pores near the chromium oxide and metal interface, which suggest defect aggregation. The pores are larger in the case of the 5 day Cr oxide. These pores are caused by agglomeration of vacancies collecting at the oxide/metal interface. These vacancies may either aggregate at discrete sinks within the interface or migrate along the interface or into the metal matrix to form cavities[38].

The Raman spectra of the oxidized Cr (Fig. 3) are characterized by the intense band at 553 cm^{-1}. This band is attributed to the bulk value for Cr_2O_3[39]. Raman peaks at 296 cm^{-1}, 351 cm^{-1}, 529 cm^{-1}, and 616 cm^{-1} can also be assigned to the Raman modes of Cr_2O_3[40,41]. There is a small band found at 1396 cm^{-1}, which is assigned to the combination band (two or more states excited simultaneously)[42]. This combination band is more pronounced after 24 h of oxidation and it loses intensity after 5 days of oxidation. Raman spectroscopy data prove that the thin oxide film on Cr substrate obtained after 24 h and 5 days of oxidation is Cr_2O_3.

DB-VEPAS

Figure 4 shows the results from the DB-VEPAS experiment on the as-polished, annealed for 24 h and 5 day samples, as well as an ultra-high vacuum (UHV) annealed Cr-reference. DB-VEPAS results are often presented in terms of S-parameter versus energy (E_p), where S is defined as the fraction of positron annihilation with free and valence electrons. More details on the definition and calculation of the S-parameter can be found in Selim (2021)[43]. Typically, decreases in the S-parameter correspond to reductions in the overall defect density in the material. The positron implantation depth is estimated according to a Makhovian implantation profile[44]. To obtain more quantitative information about defect densities across sample thickness and approximate thicknesses of the oxide layers, the VEPFit code[45,46] has been utilized. The code numerically solves the positron diffusion equation and provides characteristic parameters i.e. positron diffusion lengths and ranges of individual layers in multi-layer systems. It allows for fits of $S(E_p)$ curves for multilayered systems and provides thicknesses and effective positron diffusion lengths L_+ (a parameter inversely proportional to defect concentration) for each layer within a stack. The calculated L_+ and corresponding defected layer thicknesses are presented in Table 1.

First, a relatively well annealed (1000 °C, 10 h, at $<10^{-8}$ mbar) Cr reference sample (no oxide) is presented to give a baseline for the S-parameter of a nearly defect free material. A long positron diffusion length was obtained $L_+ \approx 130$ nm, indicating a material with only residual open volume (for a defect free metal $L_+ > 150$ nm is expected[43]). In contrast, the as-polished Cr sample exhibits an overall high defect level compared to this reference sample. There is evidence of three layers with different defect structures in the

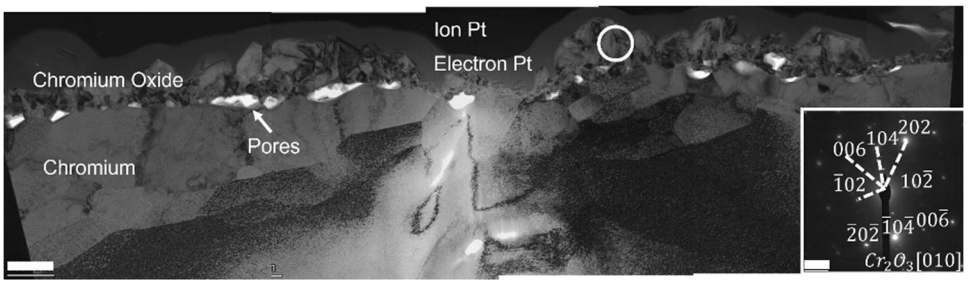

Fig. 1 TEM bright field micrograph of chromium sample oxidized in air for 24 h at 700 °C. The formation of chromium oxide (evident from selected area electron diffraction pattern) is shown as well as pores (bright white contrast) which are mostly found at the metal/oxide interface. Scale bar for TEM: 500 nm. Scale bar for SAED: 2 nm.

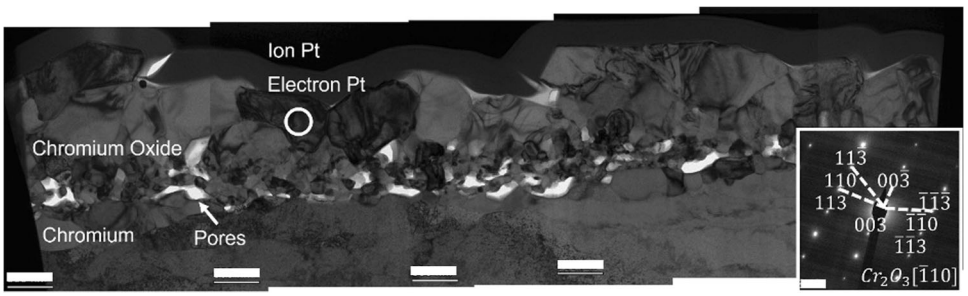

Fig. 2 TEM bright field micrograph of chromium sample oxidized in air for 5 days at 700 °C. The formation of chromium oxide (evident from selected area electron diffraction pattern) is shown as well as pores which are mostly found at the metal/oxide interface. Scale bar for TEM: 500 nm. Scale bar for SAED: 2 nm.

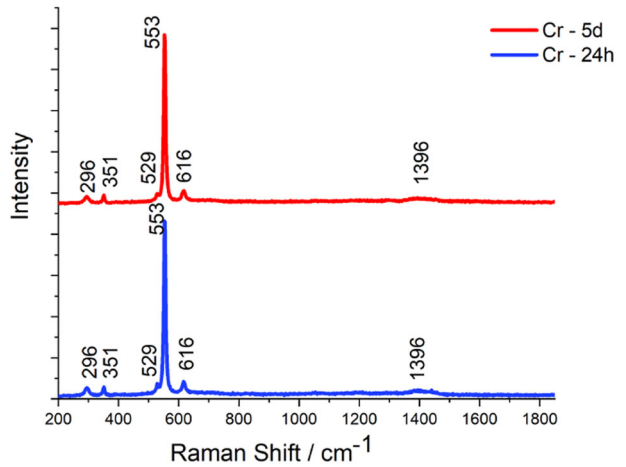

Fig. 3 Raman spectra of chromium samples oxidized at 700 °C in air for 24 h (lower, blue spectrum) and 5 days (upper, red spectrum). Both spectra were analyzed for evidence of Cr_2O_3 Raman peaks.

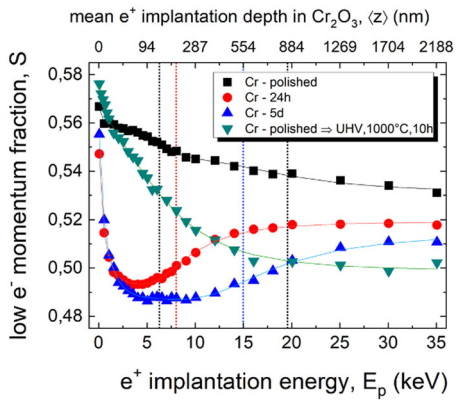

Fig. 4 DB-VEPAS results for annealed and as-polished chromium versus thermally oxidized chromium. S-parameter for a reference UHV 1000 °C, 10 h annealed Cr, as-polished Cr, and Cr oxides annealed to both 24 h and 5 d from DB-VEPAS. The curves are fitted using the VEPfit code[44] and vertical lines represent interfaces between specific regions of different open volume (Cr - polished sample) or between the oxide and Cr (oxidized samples).

subsurface region (<100 ± 20 nm) compared to the middle (<627 ± 190 nm) and deep-bulk material, which is probably due to polishing during sample preparation. This adds cold-work defects to the subsurface and middle-bulk. There is also a thin oxide layer (<10 nm) likely present after polishing. The trend of the S-parameter after the subsurface region to converge toward the bulk literature values is noted; however, the calculated L_+ of bulk suggests at least 6 times larger defect density compared to the reference sample. In order to obtain a reasonable $S(E_p)$ fit for the Cr-polished sample, a three-layer system is assumed. The lowest residuals were obtained in case of $L_+ \approx 10$, 15, and 20 nm for the sub-surface, middle, and deeper-bulk regions, respectively.

Table 1. Calculated using VEPFit code thickness, and effective diffusion lengths, L_+, for the oxidized and a reference sample.

Sample name	d_1 (nm) [oxide]	$L_{+,1}$ (nm) [oxide]	$L_{+,2}$ (nm) [substrate]
Cr – 24 h	205 ± 80	8 ± 4	44
Cr – 5d	576 ± 281	13 ± 4	119
Cr-UHV-annealed	–	–	131 ± 11

In the oxidized samples, further oxidation led to reduction of the overall defect level and clear oxide layer growth. The 24 h oxidation modified the subsurface region and annealed out the defects in the bulk, which is seen in the overall S-parameter decrease relative to the as-polished Cr. The calculated positron diffusion length $L_+ \approx 8$ nm reflects large defect density in the sub-surface oxide, which is reduced after further oxidation ($L_+ \approx 13$ nm). The shape of the 24 h and 5 day S-parameter plot suggests two layers, the sub-surface oxide and Cr-bulk, with calculated oxide thickness of 205 ± 80 nm and 576 ± 281 nm, respectively, which is in qualitative agreement with TEM (measured around 250 nm and between 500 to 1000 nm, respectively). The relatively large error (about 50%) of the calculated defected layer is a consequence of large sample roughness as well as the material density value, which has been assumed as homogenously distributed across the layer thickness. The latter is evidently lower in the porous part of the film, closer to the substrate interface. A lower effective value of density would bring the calculated oxide thickness closer to the measured by TEM. Based on these results, increasing oxidation time not only increases the oxide layer thickness, but also anneals out defects in the previous oxide layer resulting in overall lower defect concentration (24 h oxidation compared to 5 days). Similarly, defects are annealed out in bulk chromium substrate with increasing oxidation time (L_+ increases).

In the oxidized samples, the large decreases in the S-parameter in the first 50 nm are due to partial positron annihilation at surface states from back-diffused positrons. Positrons after implantation diffuse in any direction through the crystal, however, at low implantation energies, they can back diffuse to the surface and are trapped in the surface pseudo potential, where they annihilate after longer lifetimes on average compared to bulk or localized annihilation. This increases the S-parameter which accordingly scales with the positron lifetime.

VEPALS

In order to evaluate defect microstructure in the oxide layers and further characterize the decrease of defect concentration as a function of annealing time, PALS measurements were performed on the same samples. The 5 day oxidation decreased the average defect size (τ_{av}) and defect density compared to the 24 h sample (Fig. 5), in agreement with DB-VEPAS (Fig. 4). In addition, the slow decay of the average lifetime as a function of E_p in the first 50 nm

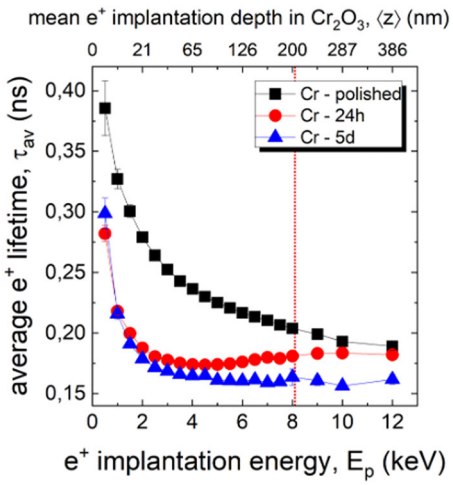

Fig. 5 Average positron lifetime τ_{av} for as-polished chromium versus thermally oxidized chromium. The red line indicates the average oxide thickness for the 24 h annealed sample. Average lifetimes and standard errors were calculated using PALSfit spectra decomposition[47].

confirms the persistent surface effects observed in the S-parameter, especially for the as-polished Cr sample.

Notably, the largest achievable $E_p = 12$ keV during PALS did not allow positrons to probe as deep as DB-VEPAS. Thus, in the 24 h sample, only the deepest implanted positrons at $E_p > 8$ keV are sampling the bulk Cr metal, resulting in the average lifetime converging toward the as-polished Cr sample. The average oxide layer thickness is marked in Fig. 5 to highlight the expected depth of the 24 h metal-oxide interface. In the case of 5 day Cr oxide, the available positron energy was not enough to implant positrons into Cr-bulk, hence the obtained signal originates purely from the oxide layer.

By fitting the PALS data using the PALSfit code[47], specific lifetimes and their relative intensities were obtained, which represent defect sizes and concentrations within the oxide layers, respectively (Fig. 6). Larger lifetimes correspond to larger defect complexes, and higher intensities of respective lifetimes reflect higher associated relative defect densities. Three lifetime components were analyzed for each sample, as seen in the left half of Fig. 6 (the third component originating from the surface ortho-positronium was omitted for clarity due to its residual intensity). As will be discussed, the first corresponds to smaller defects and/or dislocations while the second component corresponds to larger vacancy clusters.

In the as-polished Cr sample, despite the near surface effect, τ_1 monotonically decreases to about 161 ps throughout the thickness, but it shows no saturation yet. The further decrease in τ_1 is expected for larger E_p as evidenced from $S(E_p)$. The value of the bulk lifetime in Cr metal reported in the literature is 120 ps[48]. The first (161 ps) component is larger than for bulk delocalized annihilation but lower compared to the value of 184 ps for Cr monovacancy[49], suggesting this component is likely associated with positron annihilation at dislocations[50]. Dislocations act as shallow positron traps[51,52] wherein positrons have a low binding energy (10 to 100 meV)[53]. Consequently, thermal positrons are weakly localized in dislocations, and they get de-trapped and annihilate with lifetimes slightly above the bulk value. Probably, τ_1 is averaging the lifetime in bulk and at dislocations. Positron trapping at dislocations in Cr_2O_3 is probable and has been previously observed[54]. The second lifetime component τ_2 is in the range of 450 ps, indicating the presence of large vacancy clusters of more than 15 vacancies. This measurement confirms an overall high defect level from polishing in addition to the near surface effects such as partial positron annihilation at surface states from back-diffused positrons[47,55].

Figure 7 shows theoretical calculations of positron lifetimes in Cr_2O_3 for the delocalized (bulk lifetime) and localized (positrons trapped at vacancy like defects and their agglomerations) states obtained using the atomic superposition (ATSUP) method within two-component density functional theory (DFT) ab initio calculations[48]. For the electron-positron correlation, the generalized gradient approximation (GGA) scheme was used[49].

For the oxide samples, the first lifetime component τ_1 ~151 ps represents the bulk lifetime or positron annihilation at oxygen vacancies (see Fig. 7 for a reference of low order vacancy defect configurations in Cr_2O_3). It should be noted that oxygen vacancies are typically positively charged, hence repulsing to positrons, however they are positron traps if they become neutral. Considering the low L_+ obtained for oxidized films from the VEPfit $S(E_p)$ analysis, trapping at oxygen vacancies becomes a viable option. Another possibility is shallow trapping at dislocations not associated with vacancies[56]. The second lifetime component, τ_2 varies from 350 to 460 ps throughout the measured thickness of the oxide. This large lifetime indicates the presence of large vacancy clusters with more than 10 to ~25 vacancies [see Fig. 7]. This variance in lifetime values is more obvious in the oxidized samples indicating the increase of the cluster size at higher depths. Lastly, a positron lifetime representing the annihilation of surface

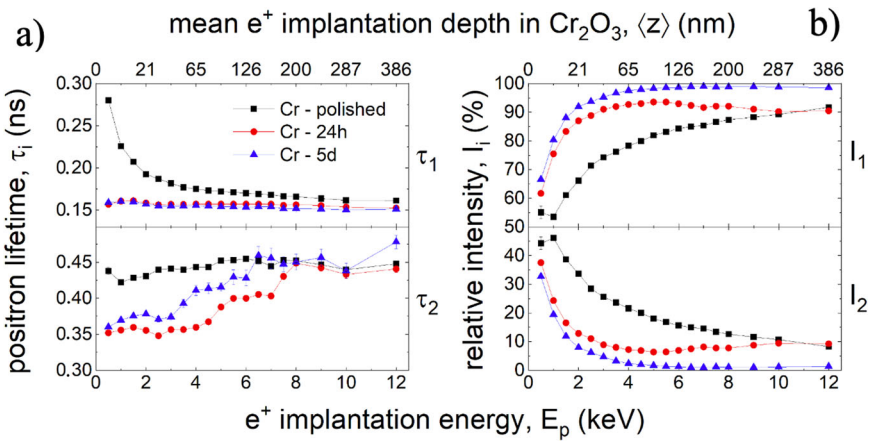

Fig. 6 VEPALS results for as-polished versus thermally oxidized chromium. Positron lifetime components τ_i (**a**), their relative intensities I_i (**b**), and standard errors were calculated from PALSfit spectra decomposition[47] for as-polished Cr versus air oxidized Cr. Most error bars are smaller than the size of the symbols used for data points representation and reside within the respective symbols.

Annihilation state	Calculated positron lifetime (ps)
Bulk	151.7
Chromium vacancy (V_{Cr})	197.4
Oxygen vacancy (V_O)	153.7

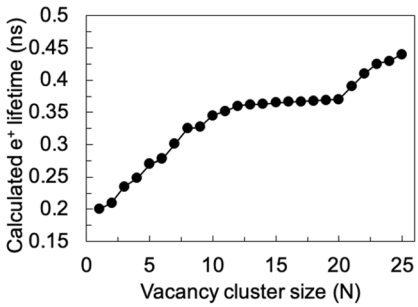

Fig. 7 ATSUP simulated annihilation states for bulk and monovacancy configurations in Cr_2O_3. Calculated positron lifetime as a function of vacancy cluster size with N agglomerated vacancies is also plotted. The spherical void was obtained by removing Cr and O atoms around a reference point and sorted by distance.

positronium τ_3 can be found in the PALS data with an intensity dropping towards zero for larger implantation depths (with decreasing influence of the surface). The fit algorithm usually shows this component even if it has intensities less than 0.5%. For PALS results, data points with less than 0.5% intensity are not shown.

Two important trends emerge from the PALS lifetime intensity data after associating τ_1 with positron annihilation in the bulk, oxygen vacancy, or dislocation states, and τ_2 with large vacancy clusters. First, aging the oxide increases the relative intensity I_1 of τ_1 up to ~100% for the 5 days of oxidation, compared to about 90% for 24 h. This strongly suggests that nearly all positrons annihilate at either the bulk Cr_2O_3 oxide, oxygen vacancies, or dislocations. Second, aged oxide layers show lower relative defect concentration. Increasing the oxidation time from 24 h to 5 days decreases the relative intensity I_2 of the defect cluster lifetime τ_2. These results confirm the trends from the DB-VEPAS data, so increasing aging oxide layers results in relatively less overall measured defects within the grown oxide. This suggests that defects anneal with aging.

DC electrochemical characterization in aqueous media

Electrochemical experiments were performed both interrogating corrosion performance of 24 h and 5 day air oxidized chromium as well as assessing electronic defects. DC electrochemical corrosion experiments were performed in aqueous (0.1 M borate buffer) solution to assess the potential dependent anodic behavior of as-polished and thermally oxidized chromium. Figure 8a shows the initial 600 seconds of open circuit potential (E_{OC}) monitoring prior to the anodic potentiodynamic polarization tests. The OCP is a mixed potential established between the anodic and cathodic half-cell reactions determined by a combination of thermodynamic and kinetic factors. All coupons displayed a stable potential trend over the duration of the experiment and varied less than 20 mV. The effect of high temperature oxidation is significant as indicated by the +150 to +200 mV shift to a nobler (more positive) potential relative to the as-polished chromium coupons. The OCP is defined by Cr oxidation and with sluggish oxygen evolution reaction (OER) current occurred starting at +0.4 V_{SCE}. The 5 day oxidized chromium exhibits the most noble potential of the three conditions. This suggests passivation is better or improved after 5 days. The OCP scan was followed by linear sweep voltammetry (LSV) using the cyclic potentiodynamic polarization test method in the range of −0.1 V to +1.0 V relative to E_{OC} as indicated in Fig. 8b.

In the anodic potential domain of the polarization scan, the as-polished coupon with a 20 nm thick and highly defective damaged layer exhibits the highest current densities followed by the 24 h air oxidized Cr, and the 5 day oxidation. The net current densities observed are dominated by the electrochemical passivation resulting in the formation of $Cr(OH)_3$[57] and CrOOH during the scan[58] coupled with sluggish oxygen evolution reaction (OER) current that starts at +0.4 V_{SCE}. It is noted that despite the borate buffer being deaerated with N_2 purging,

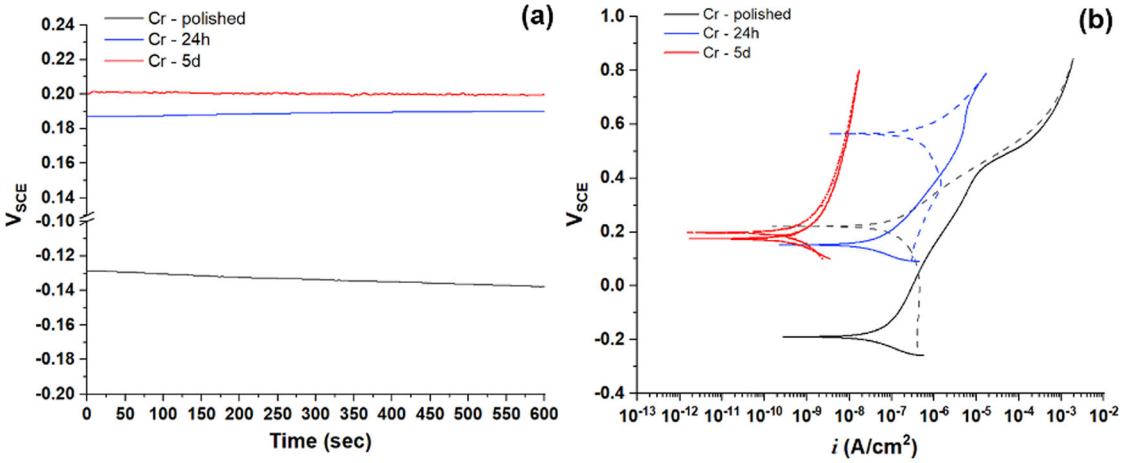

Fig. 8 Electrochemical corrosion results for as-polished versus thermally oxidized chromium. a Open circuit potential and **b** cyclic potentiodynamic polarization plot of as-polished and thermally oxidized chromium tested in 0.1 M borate buffer solution (pH 9.3) deaerated with N_2. In Fig. 9b, the solid line (-) indicates the forward scan and the dash line (–) indicates the reverse scan.

dissolved oxygen is still not completely removed[59] but is at a low background level. It is also noted that the borate buffer solution is not destructive to either the polished oxide or thermally formed oxide films[60].

The anodic polarization also causes the E_{OC} of the as-polished and 24 h air oxidized Cr to shift to a more positive potential as seen in their reverse scan. This can be explained by oxygen generated during the anodic scan due to oxygen evolution which is subsequently reduced on the downward scan. The cathodic reaction is coupled with lower anodic oxidation rate governed by oxide film point defects and increased oxide thickness. By contrast, the 5 day air oxidized Cr shows a similar E_{OC} compared to the 24 h oxidized counterpart but ~3 orders of magnitudes lower in anodic current densities. The absence of E_{OC} shift in the reverse scan also indicates that significant oxygen was not generated on the upward scan. This indicates that the chromium oxide (Cr_2O_3) formed after 5 days of air thermal oxidation is more protective towards additional oxidation as well as redox reactions (O_2 evolution from oxidation of water) on the previously oxidized surface in the borate buffer media than other variants. This is also confirmed by an additional current versus time curve under an applied +600 mV_{SCE} potentiostatic hold (Fig. 8b).

Comparison of EIS in aqueous and liquid metal media

The DC electrochemistry results presented in Section "DC electrochemical characterization in aqueous media" provide a general perspective on the electrochemical behavior of chromium covered with a thermal oxide. Additional insights regarding the electronic, semiconducting, and interface properties of those oxides were gathered via EIS. The measurements were carried out in both room temperature aqueous solution (0.1 M borate buffer, pH 9.2) and liquid metal media (LBE) at 200 °C to understand the nature of the oxide-electrolyte interaction. Figure 9a, b show the Bode plots of the 24 h and 5 day air oxidized Cr coupons in both borate buffer and LBE media, respectively. The impedance spectra of each curve were fitted with electrical equivalent circuit models (EECs) presented from Fig. 9c–e. In all cases, the capacitance term was represented as a constant phase element (*CPE*) to take into account the non-ideality of each capacitor, based on such factors as the normal distribution of oxide resistivity, surface roughness[61–63] for oxide capacitance, as well as the surface distribution of time constants for electrochemical double layer[33,64–67].

In borate buffer, the 24 h air oxidized Cr was fit with the EEC shown in Fig. 9c with a chi-square value of $6.64{\cdot}10^{-3}$. This circuit represents a superimposed outer porous and inner compact layer frequently used to characterize thermal oxides[33,62,68]. The CPE_1/R_1 represents the inner Cr_2O_3 oxide; CPE_2 represents the outer porous $Cr(OH)_3$ hydroxide; CPE_{DL}/R_{ct} represents the electrochemical double layer coupled with a charge transfer resistance (R_{ct}), i.e. faradaic reaction pertaining to aqueous oxide formation; R_1 represents the solution resistance in the pore; R_e represents the solution resistance. The EEC in Fig. 9d was used to fit the 5 day oxidized Cr coupon in borate buffer solution with a chi-square value of $7.49{\cdot}10^{-3}$. Based on the Bode plot, it is clear that the impedance behavior was dominated by a single time constant, likely physically represented by the inner layer in Fig. 9c and was thus represented by a simplified Randles circuit (Fig. 9d). The CPE_1/R_1 represents the dielectric capacitance of the oxide.

In the case of LBE, the impedance spectra of both the 24 h and 5 day oxidized Cr was fitted with a circuit of three-time constants (CPE_1/R_1, CPE_2/R_2, CPE_3/R_3) in series with the electrolyte resistance (R_e), as shown in Fig. 9e. Despite this distinction made in the fitting, the impedance spectra are remarkably similar between the two media, which should be the case since the pre-oxidization was the same and the EIS frequency range samples the time constant. Since the EIS measurement in LBE was carried out in open atmosphere at 200 °C, additional in-situ formation of Cr_2O_3 is possible in LBE. Thus, the origin of the multiple time constants may be the impedance of the Cr_2O_3 thermal oxide, as well as any new Cr_2O_3 that is formed in-situ in LBE[65] and the associated faradaic impedance associated with passivation in LBE. Along similar lines, some $Cr(OH)_3$ is likely produced instead of the thermal oxide in the borate buffer. Yet in 24 h or native oxide only a few nm of hydroxide is grown in the LSV experiment. It is noted that the EECs presented are simplified models that are mathematically representative of the impedance spectra shown in Fig. 9; the actual oxide structure is considered to be more complex (containing grains of various orientations and porosity (e.g. Figs. 1 and 2).

In both aqueous and liquid metal media, 5 day air oxidized Cr coupons behave as ideal capacitors as indicated by their high α value (e.g., Borate buffer, 0.945; LBE, 0.868-0.937) shown in Table 2. The resistive-capacitive impedance response remains relatively stable from the medium (1–10^2 Hz) to high frequency domains (10^2–10^6 Hz). The low frequency region (10^{-2}–1 Hz) is associated with the interfacial charge transfer reactions, at the oxide/metal interface coupled with the transport of charged ionic defects across oxides such as Cr^{3+} and O^{2-} responsible for aqueous passivation[32,68]. The residual oxidation in solution leads to formation of the outer oxyhydroxide over the corundum[59]. As displayed in Fig. 9a, b, the 5 day air oxidized coupon exhibits at

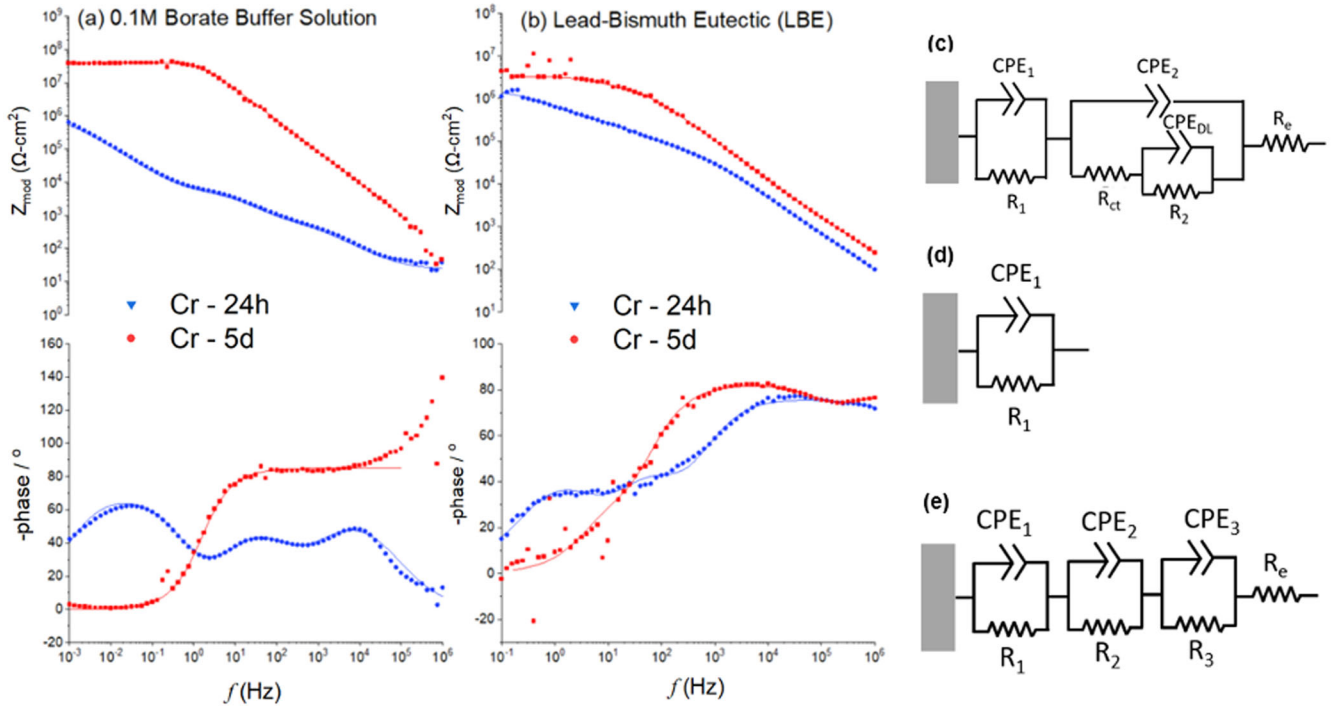

Fig. 9 Bode plots of 24 h and 5 day air oxidized chromium. Tests were conducted in **a** 0.1 M borate buffer at room temperature and **b** lead bismuth eutectic (LBE) media at 200 °C. **c**–**e** shows the representative equivalent electronic circuit (EEC) utilized to fit the impedance data shown in **a** and **b** the fits are given by the solid lines; **c** represents a dual layer oxide model consisting of an inner porous oxide; **d** represents a simplified Randles circuit consisting of a time constant; **e** represents a model with three time constants.

Table 2. The fitting parameters for impedance spectra shown in Fig. 9.

Parameter (unit)	Cr – 24 h 0.1 M Borate Buffer (Room Temperature)	Cr – 5d 0.1 M Borate Buffer (Room Temperature)	Cr – 24 h LBE (200 °C)	Cr – 5d LBE (200 °C)
CPE_1, Q (S s^{α} cm^{-2})	6.67×10^{-5}	2.93×10^{-9}	3.22×10^{-7}	6.80×10^{-8}
CPE_1, α	0.793	0.945	0.898	0.937
R_1 (Ω cm^2)	9.99×10^{5}	4.09×10^{7}	2.09×10^{3}	6.42×10^{4}
CPE_2, Q (S s^{α} cm^{-2})	4.07×10^{-6}	–	0.807	1.52×10^{-7}
CPE_2, α	0.703	–	8.96×10^{3}	0.930
R_2 (Ω cm^2)	774	–	8.08×10^{-6}	11.7
CPE_3, Q (S s^{α} cm^{-2})	–	–	0.742	3.79×10^{-7}
CPE_3, α	–	–	7.43×10^{3}	0.868
R_3 (Ω cm^2)	–	–	–	1.07×10^{6}
CPE_{DL}, Q (S s^{α} cm^{-2})	9.08×10^{-6}	–	–	–
CPE_{DL}, α	0.763	–	–	–
R_{ct} (Ω cm^2)	3.99×10^{3}	–	–	–
R_e (Ω cm^2)	24.7	–	0.276	0.649
χ^2	6.64×10^{-3}	7.49×10^{-3}	3.44×10^{-3}	1.26×10^{-3}

least an order of magnitude higher impedance modulus in both test media relative to the 24 h air oxidized coupon. Less than 1 nm of fresh oxide is grown after 5 days of oxidation and it is speculated that the point defect population and ionic mobilities are too low and the pre-oxidized layer is too thick for additional growth. It is noted that the high phase angle seen in the high frequency domain in Fig. 9a is attributed to an instrumentation artifact due to the potentiostat.

The EIS spectra of the 24 h air oxidized Cr exhibits multiple time constants in both the borate buffer (Fig. 9a) and LBE (Fig. 9b) media. The time constant in the high frequency domain (10^3–10^6 Hz) is assigned to the impedance of the oxyhydroxide layer ($R_2 = 774$ ohm-cm^2). The intermediate frequency (1–10^2 Hz) is likely a result of the impedance spectra of the Cr_2O_3 thermal oxide. The low frequency region (10^{-1}–10^{-3} Hz) represents the charge transfer reactions in parallel with the interfacial capacitance. A similar observation was seen when the coupon was exposed to LBE. Therefore, based on Fig. 9, it is clear that the chromium oxide fabricated after 24 h of air oxidation displays higher electrochemical reactivity with the oxide-forming electrolyte and potential driving force (both borate buffer and LBE) in the context of passivation than the 5 day sample.

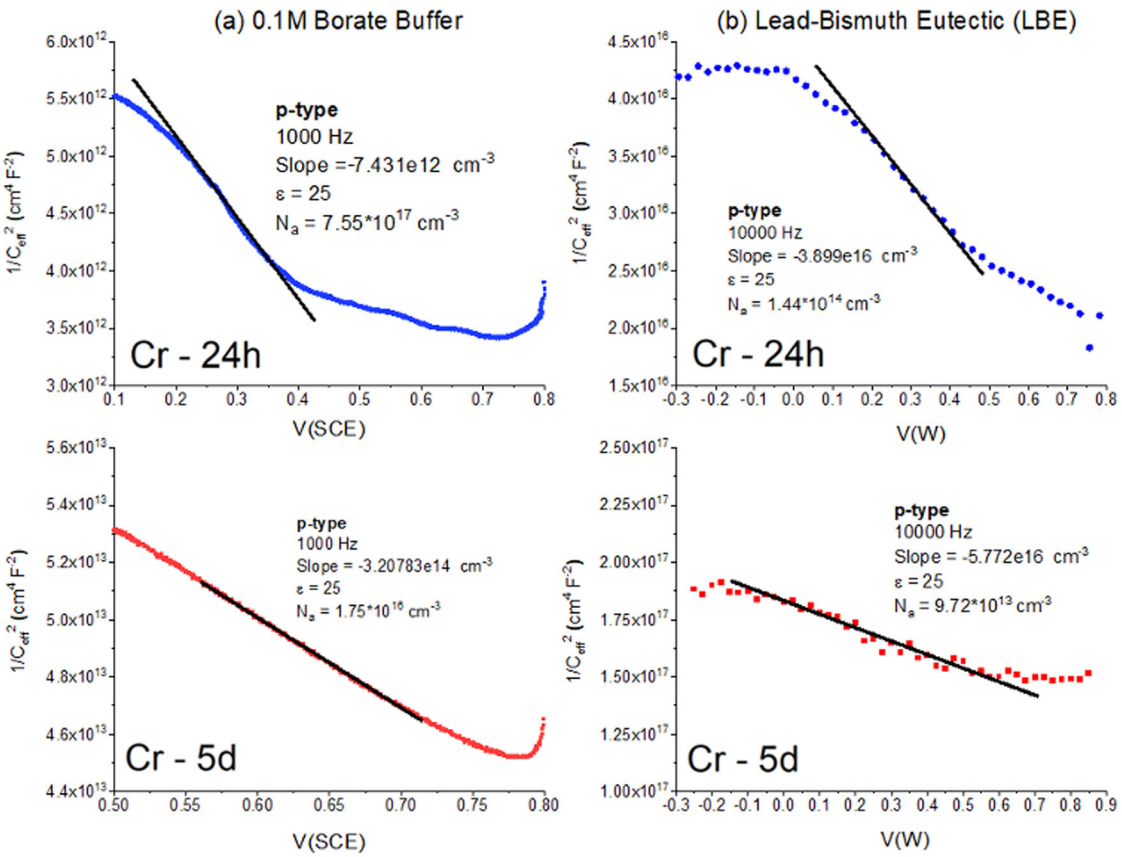

Fig. 10 Mott-Schottky plots displaying the effective capacitance ($Ceff^{-2}$) versus applied voltage of 24 h and 5 day air oxidized chromium. Tests were conducted in **a** 0.1 M borate buffer and **b** LBE. The solid line represents the linear region fitted with Eq. (2). The reference electrode was saturated calomel (SCE) in borate buffer and tungsten wire (W) in LBE. All error bars are smaller than the size of the symbols used for data points representation and reside within the respective symbols.

Given that the impedance response of the 5 day air oxidized Cr shows no significant variation in either the borate buffer or LBE environments; it can be stated that this oxide is chemically and electrochemically stable. Less than 1 nm of fresh oxide is grown after 5 days of oxidation and it is speculated that the point defect population and ionic mobilities (intrinsic property of Cr oxides) are too low and the pre-oxidized layer is too large for additional growth despite a large potential driving force. Therefore, its interface and structure were largely unaffected by the high electrochemical driving force. Following a similar argument, since the 24 h air oxidized Cr is comparatively reactive with respect to 5 day oxidation in both media, their impedance spectra becomes a function of both the existing oxide and new oxide formed in the electrolyte where their interaction is dictated by the faradaic reaction and mechanism associated with in-situ passive film formation. However, only a few nm of new oxide growth is observed. It is worth mentioning that the difference in impedance modulus magnitude of oxidized Cr coupon between borate buffer and LBE may also be affected by liquid metal wettability, reducing the total exposed area (0.6 cm^2 for LBE). This will be discussed in the next section. Given this impedance data, it is of interest to understand the origin of macroscopic electrochemical properties which are linked to microscopic point defects, and its relation to the overall stability/reactivity of the oxide covered Cr.

Mott-Schottky analysis in aqueous and liquid metal media

The Mott-Schottky (MS) plot for the oxidized chromium is shown in Fig. 10. In all cases, the effective capacitance was inversely correlated with the applied potential, indicating that the chromium thermal oxides display p-type semiconductor characteristics[69]. By the definition of a p-type semiconductor, this also suggests but does not prove that the possible ionic defects are likely metal cation vacancies and/or anion interstitials, both of which lead to compensating holes in the valence band to maintain electroneutrality[36,70]. The slope of each MS plot was extracted from the linear region in each MS plot. Based on the Mott-Schottky theory, the linear dependence of C^{-2} versus V is built upon the assumptions that (1) ionic donors with a net negative charge (such as a Cr cation monovacancy or oxygen interstitials) are the majority point defects and (2) the interface is free of faradaic/electrochemical reactions, e.g., absorbed oxygen can produce surface states (this is verified by small currents in downward scans)[70], and (3) space charge capacitance dominates the overall measured capacitance[31]. The violation of any of these conditions can lead to the departure of linearity seen in excessively high or low overpotential shown in Fig. 10.

In Fig. 10, the slope of the linear region was extracted and the acceptor densities for each test condition was calculated using Eq. (2) as shown in Table 3. The dielectric constant was assumed to be 25 in the 0.1 M borate buffer considering both the chromium oxide and oxyhydroxide layers[36,71]; and 12 in the LBE media[72]. The acceptor densities of the 24 h air oxidized Cr were found to be $7.55{\cdot}10^{17}\,cm^{-3}$ in borate buffer and $3.00{\cdot}10^{14}\,cm^{-3}$ in LBE; and the 5 day air oxidized Cr to be $1.75{\cdot}10^{16}\,cm^{-3}$ in borate buffer and $2.03{\cdot}10^{14}\,cm^{-3}$ in LBE. These concentrations are higher than in typical intrinsic semiconductors such as Si[65]. In the case of metal deficient or oxygen deficient transition metal oxides, a 1 ppm defect level would result in a concentration of about $10^{17}\,cm^{-3}$ given a lattice concentration of ~10^{23} perfect lattice site ions per cm^3.

Table 3. Dielectric constants and Ionic acceptor densities (N_A) calculated for the 24 h and 5 day air oxidized Cr in 0.1 M borate buffer and LBE electrolyte.

Parameter (unit)	Cr – 24 h 0.1 M Borate Buffer	Cr – 5d 0.1 M Borate Buffer	Cr – 24 h LBE	Cr – 5d LBE
ε (F cm^{-1})	25	25	12	12
N_A (cm^{-3})	7.55×10^{17}	1.75×10^{16}	3.00×10^{14}	1.03×10^{14}

In the literature, rapidly electrochemically grown Cr_2O_3, produced in short times as well as those synthesized by sputtering, often report higher defect concentrations by the MS approach than observed here[57,70]. In both test media, the higher acceptor densities of the 24 h air oxidized Cr suggests that it contains a higher concentration of ionic defects, possibly chromium vacancies and/or oxygen interstitials both compensated by holes[36,50,70], relative to the 5 day air oxidized counterpart. It is noted that the calculated acceptor density correlates with a simplified and general value of the point defect concentration but does not yield information regarding the exact charge state or the specific identity of the point defects.

It is noted that in both media the acceptor densities in LBE are about 2 to 3 orders of magnitude lower than those of the 0.1 M borate buffer solution. Careful considerations were taken to understand the origin of such discrepancy. Firstly, the C-E linear dependence suggests that the MS analysis is still applicable, and the use of high single frequency in a downward sweep in an environment with a high oxygen activity enables the defect population to be "frozen-in." It is also important to note that there have not been fundamental reasons proposed that have discredited the use of MS analysis in liquid metal. Secondly, due to the low wettability of LBE on oxide surfaces, it is expected that the effective surface area is reduced significantly from the original exposure surface area (0.6 cm^2). Thirdly, for the sake of a straightforward comparison between acceptor densities, only two dielectric constants (25 for borate buffer; 12 for LBE) were considered. However, realistically the thermal oxides are more complex, and the dielectric constant may need to be adjusted in accordance with its environment.

DISCUSSION

The present study sheds light on defect identities and densities as a function of oxidation time. Given the systemic and diverse approach to characterization undertaken herein, corroborating information was obtained heretofore lacking in separate computational and experimental studies and theoretical treatments. Hence it is appropriate to emphasize the complementary aspects of these experimental techniques, and their contribution in revealing the identity and concentrations of point defects during thermal oxidation and during exposure to oxidizing media, i.e., aqueous borate buffer and liquid metal. This information is often obtained using disparate methods but is uncorroborated. To address this gap, we first present a summary of the findings associated with each technique:

- 24 h and 5 day Cr oxides are confirmed to be Cr_2O_3. (Raman/TEM)
- Oxidation time introduces larger pores near the metal oxide interface. (TEM)
- Oxidation time increases oxide layer thickness. (TEM/PAS)
- Oxidation time increases grain size near the oxide surface, and smaller grains exist closer to the metal/oxide interface, pointing to an annealing effect. (TEM)
- Total oxide defect population decreases with increasing oxidation time. (PAS)
- The relative density of vacancy clusters in the oxides decreases with oxidation time. (PAS)
- Cation chromium monovacancies are not found in Cr_2O_3. (PAS)
- The 5 day Cr oxide is more electrochemically stable in both aqueous and liquid metal media than the 24 h oxide. (Echem)
- Mott-Schottky results show that both Cr oxides display p-type character. (Echem)
- The 5 day Cr oxide shows lower charge carrier density than the 24 h sample. (Echem)

With this basis, we can more accurately understand the atomistic origin of the reduced defect densities of chromium oxides formed during longer air oxidation. Based on TEM results, it was observed that voids aggregated at the metal/oxide interface, which could act as a vacancy source for non-equilibrium point defects[73–75]. Since the chromium coupons were polished to 1200 grit (P-4000) surface finish, the entire coupon surface is cold worked, which creates dislocations that act as sinks for point defects. This finding is strengthened by the PAS analysis showing much larger values of the S-parameter in the polished versus polished and UHV-annealed sample (Fig. 4). Also, the TEM micrographs showing that the voids formed due to numerous defects did not migrate to the bulk chromium substrate (Figs. 1 and 2). In this case, the measured acceptor density agrees with the intrinsic point defect equilibrium concentration such as 10^{-6}% at high P_{O2} and 1100 °C[11–13]. Moreover, it is noted that Cr_2O_3 volatilization to CrO_3 and Cr is excluded in this discussion since these phenomena do not occur extensively until reaching 900 °C, although it could still occur to a limited degree at lower temperature[32,33].

An important observation is that positron annihilation spectroscopy (DB-VEPAS and PALS) and electrochemical measurements both consistently showed lower defect densities in 5 day air oxidized chromium than in the 24-hour sample. In other words, both fundamentally different experimental techniques can measure point defects separately with mutually complementary results. For positron annihilation lifetime spectroscopy (PALS), the positron lifetime signal pertaining to large vacancy clusters defects vanished from $I_2 \approx 10\%$ to zero comparing 24 h to 5 days of air oxidation, so no large vacancy clusters are observed in the 5 day sample at the same oxide layer depth. The PALS technique provides information about the size of neutral and negatively-charged vacancies, and although larger vacancy clusters were observed in these oxides, exactly which particular charge state cannot be probed. Isolated cation vacancies would be negatively charged and seen by PALS.

Combining the analysis from Mott-Schottky and PALS reveals insight into the predominant defect species within the oxide. Mott-Schottky analysis indicates the p-type semiconductor character of the chromium thermal oxides with close to an order of magnitude decrease in acceptor densities after 5 days of air oxidation. The percent decrease measured through electrochemical technique (~98% decrease in borate and ~33% decrease in LBE) agrees qualitatively with the relative percent decrease in measured defects found from PALS technique. The data suggests that oxygen interstitials and larger chromium vacancy clusters could provide charge carriers in the 24 h oxide. Longer oxidation time (5 days) may anneal larger vacancy-type defects and leave oxygen interstitials as the predominant defect type, which could

be the reason for the order of magnitude decrease in acceptor densities after 5 days of air oxidation.

PAS also shows a high concentration of Cr vacancy related defects in 24 h, which could provide holes contributing to the charge transport. For the 5 day sample, many of these chromium larger vacancy defects could be annealed and therefore provide more oxygen interstitials, but the acceptor concentration did not increase. So even though both cation vacancy related defects and oxygen interstitials provide holes, for the 5d sample, if chromium vacancy clusters were annealed, oxygen interstitials became the dominant acceptors driving the transport.

Density functional theory calculations performed by multiple authors[18–21] are divided on whether chromium or oxygen point defects are predominant within the oxide, be it vacancies, interstitials, or even Frenkel defects (composed by an interstitial atom and a vacancy). From the Mott-Schottky analysis, p-type behavior provides evidence that either chromium vacancies or oxygen interstitials are predominant. PALS experiments show no evidence of isolated chromium cation monovacancies in the oxide, even though cation monovacancies are negatively charged and readily observable by positrons, which leaves oxygen interstitials or larger chromium vacancy clusters as the likely predominant point defect types. In the DFT calculated migration energies, oxygen interstitials are also shown to be relatively more stable defects because contrary to the large lattice spacings generated by chromium monovacancies, oxygen interstitials do not generate considerable local structural distortions to the lattice. This results in oxygen interstitials' low migration energy barrier[21], which would be necessary to drive diffusion and migration, especially compared to chromium vacancies' high migration energies[20–23].

However, both electrochemical and positron annihilation-based techniques do not prove the predominance or quantify the absolute population of oxygen interstitials, which may be the origin of this discrepancy in terms of measured point defect populations. For reference, the thermal equilibrium concentration of oxygen interstitials in Cr_2O_3 at 700 °C was calculated using the migration and formation enthalpies from DFT simulations[22] resulting in on the order of 10^{13} interstitials per cm^3, which is less than the Mott-Schottky acceptor density after 5 days of oxidation. Even though 5 days of oxidation does not match thermal equilibrium conditions, the acceptor density at longer oxidation time trends toward the thermal equilibrium concentration, indicating that this oxide is significantly closer to equilibrium than the 24 h sample.

Positron annihilation spectroscopy and electrochemistry supports, but does not prove, the primary role of chromium vacancy cluster complexes and/or anion oxygen interstitials in dictating transport in Cr_2O_3 in thermally oxidizing environments. Positron spectroscopy results suggest the presence of larger vacancy cluster complexes within the oxide, which can provide charge carriers. When oxidizing a pure chromium coupon, the partial pressure of oxygen (P_{O2}) plays a critical role in dictating the semiconductor properties of Cr_2O_3 during oxidation, in particular, which point defect type dominates the oxidation diffusion process. At low P_{O2} (e.g., air oxidation), the outward transport of Cr interstitials dominates (n-type character)[16,21,76,77]; whereas at high P_{O2}, chromium vacancies dominate (p-type character)[16,21,76,77], but at the metal-oxide interface, relative oxygen mobility is significantly higher than that of Cr[22].

On the contrary, when Cr_2O_3 is exposed to oxidizing environments that are of interest to corrosion, the P_{O2} level is typically low and fixed because they are in equilibrium with the atmosphere. The driving force and its point defect transport mechanism (limited to charged point defects) are thus electrochemical and are dictated by the potential drop across the metal/oxide, oxide/electrolyte interfaces and the oxide thickness itself. High applied potentials enable such potential drops. The point defect transport mechanism has also been investigated under the point defect model (PDM), which is one of the macroscopic aqueous passivation models that bridges between the role of point defects and oxide formation from a kinetic point of view[35]. Additional reviews were carried out by the Marcus group summarizing these established models[78]. The same group also outlined a complete model of oxide film growth kinetics, which will not be discussed in detail here[76]. It is important to note that the potential drop across the metal/electrolyte interface relates to surface potential applied or by anodic potentiostatic polarization[79–81].

When exposed to either borate buffer or LBE, the in-situ formation of either $Cr(OH)_3$ in borate buffer or additional Cr_2O_3 or CrO_3 in LBE were detected from linear sweep voltammetry. Based on established models[20,35,37,82] as well as results presented here, the transport (by migration in thin film high field models) of oxygen interstitials could be expected to dominate such local passivation process. The oxygen interstitials or chromium vacancy cluster complexes are suggested to be the dominant defects resulting from air oxidation in atmospheric conditions.

On the basis that (i) no significant amount of chromium monovacancies were generated during electrochemical measurements as is typical of passivation of freshly polished surfaces; (ii) the 5 day air oxidized chromium contains slightly less point defects but roughly twice the thickness relative to the 24 h counterpart, it may be concluded that the electromigration flux of charge carriers within the 5 day oxide is significantly lower due to higher oxide thickness and lower defect content (thus lower strength of electric field), leading to the three orders of magnitude drop in DC current density observed in Fig. 8b and overall improved electrochemical stability. Based on this drop in current density, in the case of thermal oxides on pure chromium, both the thickness factor and point defect density could have a strong influence in dictating the electrochemical/corrosion behavior of the oxides.

The main purpose of this study is to utilize multiple complimentary characterization techniques to evaluate the types of defects, ionic point defect densities, and agglomeration of defects during growth of Cr oxide layers in a single study. Defect concentration was determined using positron annihilation spectroscopy, Mott-Schottky analysis, and electrochemical techniques as well as TEM for larger scale defect structures. This approach allows a comprehensive view on the defects in thermally grown oxides. It was found that, while the oxide layer increases in thickness as a function of oxidation time, the defect density is greatly reduced. The most likely predominant defects were identified as oxygen interstitials or chromium vacancy cluster complexes, and these are responsible for the ionic transport. This confirms the growth process for Cr_2O_3 is dependent on the transport of oxygen interstitials and chromium vacancy clusters while adding quantitative data to the process.

METHODS

Sample preparation

Polished Cr samples (1200 grit) were oxidized in air at 700 °C for 24 hours (24 h) and 5 days (5 d) using a box furnace. The entire sample treatment flow through the experimental procedures is shown in Fig. 11. It is important to note that it was always the exact same traveling chromium coupon (sample) that underwent the different characterization techniques.

TEM and Raman spectroscopy

An as-polished Cr sample was kept for reference. Characterization efforts began with PAS to quantify vacancy and vacancy-related defect content. After PAS investigations, the chemical compositions and structures of the oxide scales on the thermally oxidized chromium were characterized by TEM. TEM thin foils were cut from the oxide layer of the thermally oxidized samples using a ThermoFisher Quanta 3D field emission gun focused ion beam (FIB) instrument. TEM was conducted using a ThermoFisher Talos

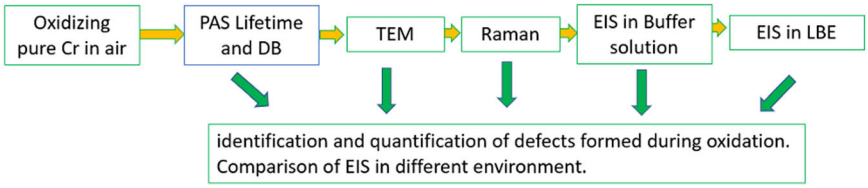

Fig. 11 Sample flow through the experimental procedure. The same oxidized chromium samples traveled among experimental facilities for the different characterization techniques.

F200X with a field emission gun operating at 200 kV. A Renishaw InVia™ Confocal Raman microscope was utilized for chromium oxide layer confocal Raman spectroscopy measurements, featuring a 514 nm laser (low power – 10%) with 1800 lines per millimeter diffraction grating and 50x long focal length. A small region of the sample was inspected before and after analysis by optical microscopy to ensure no laser-induced oxidation had occurred.

Positron annihilation spectroscopy

The samples were sent to the Institute of Radiation Physics at Helmholtz-Zentrum Dresden – Rossendorf (HZDR) for positron annihilation spectroscopy (PAS) to characterize the defect type and density at different depths within the grown oxide layers. DB-VEPAS measurements were conducted at the apparatus for in-situ defect analysis (AIDA)[83] on the slow positron beamline (SPONSOR)[84]. Positrons were implanted into each sample with discrete kinetic energies E_p in the range between 0.05 and 35 keV, which allows for depth profiling from the surface down to about 2 µm.

Depth-resolved variable energy positron annihilation lifetime spectroscopy (PALS) was also done to assess defect microstructure of the oxide layers grown at different conditions. Positron implantation energies were varied here from 0.5 – 12 keV in 0.5 keV increments, probing over the first ~380 nm of the samples. The PALS experiments were performed at the mono-energetic positron spectroscopy (MePS) beamline, which is one of the end stations of the radiation source ELBE (Electron Linac for beams with high Brilliance and low Emittance) at HZDR (Germany)[85,86]. A $CrBr_3$ scintillator detector coupled to a Hamamatsu R13089 PMT was utilized for the gamma quanta acquisition and the signals were processed by SPDevices ADQ14DC-2X digitizer[73]. The time resolution function achieved a value of about 0.230 ns. The resolution function required for spectrum analysis includes two Gaussian functions with distinct intensities and relative shifts, which both depend on the positron implantation energy, E_p. All spectra contained at least 10^7 counts. Typical lifetime spectrum $N(t)$ is described by Eq. 1:

$$N(t) = \sum \left(\frac{1}{\tau_i}\right) \mathrm{I_i} \exp\left(-\frac{t}{\tau_i}\right) \quad (1)$$

where τ_i and I_i are the positron lifetime and intensity of the i-th component, respectively, and the sum of intensities, I_i, must be equal to one[47]. Spectra were deconvoluted into a few discrete lifetime components using the PALSfit software[47], which directly show evidence of different defect types (sizes) and their corresponding relative intensities, quantifying the overall concentration of each defect type.

Electrochemical measurements

To understand the corrosion and semiconducting properties of the as-oxidized chromium metals, the electrochemical behavior of these coupons in an analytical grate borate buffer aqueous electrolyte (0.1 M $Na_2B_4O_7{\cdot}10H_2O$, pH = 9.2, 20 °C) and a lead-bismuth eutectic liquid metal electrolyte (45.5 wt.% Pb-55.5 wt.% Bi, 200 °C) was compared.

A conventional three-electrodes cell was used for the aqueous electrochemical experiments, with a Pt mesh as the counter electrode, a saturated calomel electrode (SCE) as the reference electrode, and the oxidized Cr metals as the working electrode. The three-electrodes cell was then connected to a Gamry 600 + ™ potentiostat utilized for electrochemical measurements. Prior to each test, deaeration was performed by bubbling industry grade N_2 directly to the aqueous electrolyte for 30 minutes, and the N_2 bubbling was continued throughout the duration of the test. In the borate buffer solution, two separate measurements were performed: (i) a 600 s open circuit potential (E_{OC}) scan, followed by an EIS scan at E_{OC} in the frequency range between 1 mHz and 1 MHz at 8 point per decade with a 10 mV sinewave perturbation, and ended with a potentiodynamic polarization (PD) scan from −0.1 to +1.0 V relative to E_{OC} at a scan rate of 0.5 mV per second; (ii) a 600 s open circuit potential (E_{OC}) scan, followed by a Mott-Schottky analysis performed by sweeping the potential from +0.8 V to +0.1 V versus E_{OC} at a single frequency of 1000 Hz. The step size was 5 mV. The potential range represents the passive region of the coupons determined from their PD scans, whereas the measurement frequency was determined from the E_{OC} impedance spectra representing the frequency dominated by oxide capacitance at a relatively constant phase angle. This was carefully selected to avoid effects pertaining to leakage current due to faradaic reactions or distribution of the densities of states within the oxide. For the electrochemical experiments in lead bismuth eutectic (LBE), we also chose a three-electrodes system. A tungsten wire with a diameter of 0.5 mm was used as the reference electrode (RE). The 304 L stainless steel crucible was connected to the counter electrode (CE). To avoid repetition, details of the experiments can be found in[87]. Two separate measurements were performed in LBE: (i) a 600 s open circuit potential (E_{OC}) scan, followed by an EIS scan at E_{OC} in the frequency range between 1 MHz and 0.1 Hz at 8 point per decade and a 10 mV sinewave perturbation. (ii) a 600 s open circuit potential (E_{OC}) scan, followed by a Mott-Schottky analysis performed by sweeping the potential from +0.85 V to −0.3 V versus E_{OC} at a single frequency of 1000 Hz. The step size was 20 mV.

The semiconductor properties of the chromium thermal oxides with respect to the solid/electrolyte interface can be analyzed through the Mott-Schottky method. When a semiconductor, i.e., oxide, is exposed to the electrolyte, equilibration of the Fermi energies between oxide and electrolyte (i.e., redox potential) results in the transport of electrons across the solid/electrolyte interface to equalize the Fermi energies, i.e., this creates band bending in the band energy landscape in the semi-conductor oxide. Band bending results in an electron depleted or accumulated region, yielding a dielectric capacitance known as the space charge capacitance (C_{SC}), which can be estimated from electrochemical techniques. The space charge capacitance can be extracted by the Mott-Schottky equation under the assumption of Boltzmann distribution of electrons within the oxide and electroneutrality is ensured across the solid/electrolyte interface through Gauss's Law[69].

$$\frac{1}{C_{SC}^2} = \frac{2}{\epsilon\epsilon_0 e N_A}\left(V - V_{FB} - \frac{kT}{e}\right) \text{For a p} - \text{type semiconductor} \quad (2)$$

$$\frac{1}{C_{SC}^2} = \frac{-2}{\epsilon\epsilon_0 e N_D}\left(V - V_{FB} - \frac{kT}{e}\right) \text{For an n} - \text{type semiconductor} \quad (3)$$

Where ϵ_0 represents the permittivity of free space $8.85{\cdot}10^{-14}$ Fper cm, ϵ represents the dielectric constant of the oxide, N_D (N_A) is the donor (acceptor) densities, V is the applied potential, V_{FB} is the flat band potential, k is the Boltzmann constant, e is the electron charge, and T is the absolute temperature.

Based on Eqs. 2 and 3, the electronic donor/acceptor densities (N_D or N_A) and flat band potential (V_{FB}) can be extracted from the slope and intercept of Eq. 2 or Eq. 3, respectively. The Mott-Schottky analysis was carried out by measuring the capacitive impedance response at each bias voltage within the electrochemically passive region of an oxide in a given electrolyte. Therefore, when such a measurement is performed in an electrochemical system, the effective capacitance, C_{eff}, needs to be considered:

$$\frac{1}{C_{eff}} = \frac{1}{C_{CS}} + \frac{1}{C_{DL}} \quad (4)$$

where C_{DL} is the double layer capacitance. In aqueous electrolyte, C_{DL} is typically on the order of ~10^2 µF per cm relative to C_{SC}, which is on the order of ~10^{-3} µF per cm. Thus, the C_{DL} term is often neglected. Additionally, the concept of an electrochemical double layer does not apply in the case of liquid metal. Therefore, the space charge capacitance is considered the effective capacitance in both cases. It is also noted that the dielectric capacitance of the oxide is often considered as the space charge capacitance (i.e., $C_{SC} \sim C_{OX}$).

DATA AVAILABILITY

The data that support these findings are available upon reasonable request to the authors.

Received: 4 February 2022; Accepted: 16 June 2022;
Published online: 26 July 2022

REFERENCES

1. Tedmon, C. S. Jr The effect of oxide volatilization on the oxidation kinetics of Cr and Fe-Cr alloys. *J. Electrochem. Soc.* **113**, 766 (1966).
2. Lillerud, K. P. & Kofstad, P. On High Temperature Oxidation of Chromium: I. Oxidation of annealed, thermally etched chromium at 800–1100 C. *J. Electrochem. Soc.* **127**, 2397 (1980).
3. Kofstad, P. & Lillerud., K. P. On High Temperature Oxidation of Chromium: II. Properties of and the oxidation mechanism of chromium. *J. Electrochem. Soc.* **127**, 2410 (1980).
4. Gulbransen, EarlA. & Kenneth, F. Andrew Kinetics of the Oxidation of Chromium. *J. Electrochem. Soc.* **104**, 334 (1957).
5. Giletti, B. J. & Hess, K. C. Oxygen Diffusion in Magnetite. *Earth Planet. Sci. Lett.* **89**, 115–122 (1988).
6. Kaspar, T. C. et al. Bulk and Short-Circuit Anion Diffusion in Epitaxial Fe_2O_3 Films Quantified Using Buried Isotopic Tracer Layers. *Adv. Mater. Interfaces* **8**, 2001768 (2021).
7. Legrand, M., Diawara, B., Legendre, J. J. & Marcus, P. Three-Dimensional Modelling of Selective Dissolution and Passivation of Iron-Chromium Alloys. *Corros. Sci.* **44**, 773–790 (2002).
8. Diawara, B., Legrand, M., Legendre, J. J. & Marcus, P. Use of Quantum Chemistry Results in 3D Modeling of Corrosion of Iron- Chromium Alloys. *J. Electrochem. Soc.* **151**, B172–B178 (2004).
9. Diawara, B., Beh, Y. A. & Marcus, P. Nucleation and Growth of Oxide Layers on Stainless Steels (FeCr) Using a Virtual Oxide Layer. *Model. J. Phys. Chem. C.* **114**, 19299–19307 (2010).
10. Sabioni, A. C. S., Huntz, A. M., Philibert, J., Lesage, B. & Monty, C. Relation Between the Oxidation Growth Rate of Chromia Scales and Self-Diffusion in Cr_2O_3. *J. Mater. Sci.* **27**, 4782–4790 (1992).
11. Sabioni, A., Lesage, B., Huntz, A., Pivin, J. & Monty, C. Self-Diffusion in Cr_2O_3 I. Chromium Diffusion in Single Crystals. *Philos. Mag. A* **66**, 333–350 (1992).
12. Sabioni, A., Huntz, A., Millot, F. & Monty, C. Self-Diffusion in Cr_2O_3 II. Oxygen Diffusion in Single Crystals. *Philos. Mag. A* **66**, 351–360 (1992).
13. Sabioni, A., Huntz, A., Millot, F. & Monty, C. Self-diffusion in Cr_2O_3 III. Chromium and Oxygen Grain-Boundary Diffusion in Polycrystals. *Philos. Mag. A* **66**, 361–374 (1992).
14. Latu-Romain, L. et al. Towards the Growth of Stoichiometric Chromia on Pure Chromium by the Control of Temperature and Oxygen Partial Pressure. *Corros. Sci.* **126**, 238–246 (2017).
15. Huntz, A. M. & Tsai, S. C. Diffusion in Oxide Scales: Application to Cr_2O_3 Scales. *J. Mater. Sci. Lett.* **13**, 821–825 (1994).
16. Kofstad, P. & Lillerud, K. Chromium Transport Through Cr_2O_3 Scales I. On Lattice Diffusion of Chromium. *Oxid. Met.* **17**, 177–194 (1982).
17. Tsai, S., Huntz, A. & Dolin, C. Growth Mechanism of Cr_2O_3 Scales: Oxygen and Chromium Diffusion, Oxidation Kinetics and Effect of Yttrium. *Mater. Sci. Eng. A* **212**, 6–13 (1996).
18. Hoshino, K. & Peterson, N. Cation Self-Diffusion in Cr_2O_3. *J. Am. Ceram. Soc.* **66**, c202–c203 (1983).
19. Schmucker, E. et al. Oxidation of Ni-Cr Alloy at Intermediate Oxygen Pressures. I. Diffusion Mechanisms Through the Oxide Layer. *Corros. Sci.* **111**, 467–473 (2016).
20. Lebreau, F., Islam, M. M., Diawara, B. & Marcus, P. Structural, magnetic, electronic, defect, and diffusion properties of Cr_2O_3: A DFT+ U study. *J. Phys. Chem. C.* **118**, 18133–18145 (2014).
21. Medasani, B. K., Sushko, M. L., Rosso, K. M., Schreiber, D. K. & Bruemmer, S. M. Temperature dependence of self-diffusion in Cr_2O_3 from first principles. *J. Phys. Chem. C.* **123**, 22139–22150 (2019).
22. Medasani, B., Sushko, M. L., Rosso, K. M., Schreiber, D. K. & Bruemmer, S. M. First-principles investigation of native interstitial diffusion in Cr_2O_3. *J. Phys. Chem. C.* **122**, 12984–12993 (2018).
23. Gray, C., Lei, Y. & Wang, G. Charged vacancy diffusion in chromium oxide crystal: DFT and DFT+ U predictions. *J. Appl. Phys.* **120**, 215101 (2016).
24. Čížek, J. Characterization of lattice defects in metallic materials by positron annihilation spectroscopy: A review. *J. Mater. Sci. Technol.* **34**, 577–598 (2018).
25. Slugeň, V. et al. Radiation Damage of Reactor Pressure Vessel Steels Studied by Positron Annihilation Spectroscopy—A Review. *Metals* **10**, 1378 (2020).
26. Krsjak, V., Degmova, J., Sojak, S. & Slugen, V. Effects of displacement damage and helium production rates on the nucleation and growth of helium bubbles–Positron annihilation spectroscopy aspects. *J. Nucl. Mater.* **499**, 38–46 (2018).
27. Kuramoto, E., Takano, Y., Kikuchi, N. & Takenaka, M. Positron annihilation lifetime measurements of irradiated iron and iron-chromium alloys. *J. Nucl. Mater.* **141**, 829–836 (1986).
28. Lambrecht, M. & Malerba, L. Positron annihilation spectroscopy on binary Fe–Cr alloys and ferritic/martensitic steels after neutron irradiation. *Acta Mater.* **59**, 6547–6555 (2011).
29. Horodek, P., Siemek, K., Kobets, A. G., Kulik, M. & Meshkov, I. N. Positron beam and RBS studies of thermally grown oxide films on stainless steel grade 304. *Appl. Surf. Sci.* **333**, 96–103 (2015).
30. Yabuuchi, A., Maekawa, M. & Kawasuso, A. Vacancy defects in a stress-corrosion-cracked Type 304 stainless steel investigated by positron annihilation spectroscopy. *J. Nucl. Mater.* **419**, 9–14 (2011).
31. Orazem, M. E. & Tribollet, B. Electrochemical impedance spectroscopy. (Wiley, 2008).
32. Gelderman, K., Lee, L. & Donne, S. W. Flat-band potential of a semiconductor: using the Mott–Schottky equation. *J. Chem. Educ.* **84**, 685 (2007).
33. Wielant, J., Goossens, V., Hausbrand, R. & Terryn, H. Electronic properties of thermally formed thin iron oxide films. *Electrochim. Acta* **52**, 7617–7625 (2007).
34. Yu, X.-X., Han, J., Scully, J. R. & Marks, L. D. Oxygen injection during fast vs slow passivation in aqueous solution. *Acta Mater.* **213**, 116898 (2021).
35. Macdonald, D. D. The history of the Point Defect Model for the passive state: A brief review of film growth aspects. *Electrochim. Acta* **56**, 1761–1772 (2011).
36. Moffat, T. P., Yang, H., Fan, F. F. & Bard, A. J. Electron-Transfer Reactions on Passive Chromium. *J. Electrochem. Soc.* **139**, 3158–3167 (1992).
37. Atkinson, A. Wagner Theory and Short Circuit Diffusion,. *Mater. Sci. Technol.* **4**, 1046–1051 (1988).
38. Evans, H. E. Cavity formation and metallurgical changes induced by growth of oxide scale. *Mater. Sci. Technol.* **4**, 1089–1098 (1988).
39. Punugupati, S., Narayan, J. & Hunte, F. Room temperature ferromagnetism in epitaxial Cr2O3 thin films grown on r-sapphire. *J. Appl. Phys.* **117**, 193907 (2015).
40. Mohammadtaheri, M., Yang, Q., Li, Y. & Corona-Gomez, J. The effect of deposition parameters on the structure and mechanical properties of chromium oxide coatings deposited by reactive magnetron sputtering. *Coatings* **8**, 111 (2018).
41. Shim, S. H., Duffy, T. S., Jeanloz, R., Yoo, C. S. & Iota, V. Raman spectroscopy and x-ray diffraction of phase transitions in Cr_2O_3 to 61 GPa. *Phys. Rev. B: Condens. Matter* **69**, 144107 (2004).
42. Yang, J., Martens, W. N. & Frost, R. L. Transition of chromium oxyhydroxide nanomaterials to chromium oxide: a hot-stage Raman spectroscopic study. *J. Raman Spectrosc.* **42**, 1142–1146 (2011).
43. Selim, F. A. Positron annihilation spectroscopy of defects in nuclear and irradiated materials- a review. *Mater. Charact.* **174**, 110952 (2021).
44. Asoka-Kumar, P. & Lynn, K. G. Implantation profile of low-energy positrons in solids. *Appl. Phys. Lett.* **57**, 1634–1636 (1990).
45. Van Veen, A. et al. VEPFIT applied to depth profiling problems. *Appl. Surf. Sci.* **85**, 216–224 (1995).
46. Veen, A. V., Schut, H., Vries, J. D., Hakvoort, R. A. & Ijpma, M. R. Analysis of positron profiling data by means of "VEPFIT". *AIP Conf. Proc.* **218**, 171–198 (1991).
47. Olsen, J. V., Kirkegaard, P., Pedersen, N. J. & Eldrup, M. PALSfit: A new program for the evaluation of positron lifetime spectra,. *Phys. Status Solidi C.* **4**, 4004–4006 (2007).
48. Johansson, J., Vehanen, A., Yli-Kauppila, J., Hautojärvi, P. & Moser, P. Positron lifetime measurements on electron-irradiated chromium. *Radiat. Eff.* **58**, 31–33 (1981).
49. Robles, J. M., Campillo, E., Ogando & Plazaola, F. Positron Lifetime Calculation for the Elements of the Periodic Table. *J. Phys.: Condens. Matter* **19**, 176222 (2007).
50. Čížek, J., Melikhova, O., Barnovská, Z., Procházka, I. & Islamgaliev, R. K. Vacancy clusters in ultra fine grained metals prepared by severe plastic deformation. *J. Phys.: Condens. Matter,* **443**, 012008 (2013).
51. Häkkinen, H., Mäkinen, S. & Manninen, M. Positron states in dislocations: shallow and deep traps. *Europhys. Lett.* **9**, 809 (1989).
52. Linderoth, S. & Hidalgo, C. Direct evidence for positron annihilation from shallow traps. *Phys. Rev. B: Condens. Matter* **36**, 4054 (1987).
53. Chen, Z. Q., Hu, X. W. & Wang, S. J. Positron annihilation studies of defect properties in semi-insulating GaAs. *Phys. Status Solidi A* **156**, 277–284 (1996).
54. Kosub, T. et al. Purely antiferromagnetic magnetoelectric random access memory. *Nat. Commun.* **8**, 1–7 (2017).
55. Troev, T., Mincov, I., Shofan, A. & Angelov, C. Positron lifetime and Doppler broadening of annihilation gamma-line measurements in neutron irradiated chromium. *Phys. Lett. A* **140**, 147–150 (1989).
56. Assali, S. et al. Vacancy complexes in nonequilibrium germanium-tin semiconductors. *Appl. Phys. Lett.* **114**, 251907 (2019).
57. Kelsall, G. H., House, C. I. & Gudyanga, F. P. Chemical and electrochemical equilibria and kinetics in aqueous Cr(III)/Cr(II) Chloride solutions. *J. Electroanal. Chem. Interfacial Electrochem.* **244**, 179–202 (1988).

58. Marijan, D. & Gojić, M. Electrochemical study of the chromium electrode behaviour in borate buffer solution. *J. Appl. Electrochem.* **32**, 1341–1346 (2002).
59. Butler, I. B., Schoonen, M. A. A. & Rickard, D. T. Removal of dissolved oxygen from water: A comparison of four common techniques. *Talanta* **41**, 211–215 (1994).
60. Han, J. et al. Electrochemical stability, physical, and electronic properties of thermally pre-formed oxide compared to artificially sputtered oxide on Fe thin films in aqueous chloride. *Corros. Sci.* **186**, 109456 (2021).
61. Martini, E. M. & Muller, I. L. Characterization of the film formed on iron in borate solution by electrochemical impedance spectroscopy. *Corros. Sci.* **42**, 443–454 (2000).
62. Hirschorn, B. et al. Constant-phase-element behavior caused by resistivity distributions in films: I. Theory. *J. Electrochem. Soc.* **157**, C452 (2010).
63. Alexander, C. L., Tribollet, B. & Orazem, M. E. Contribution of surface distributions to constant-phase-element (CPE) behavior: 1. Influence of roughness. *Electrochim. Acta* **173**, 416–424 (2015).
64. Brug, G. J., van den Eeden, A. L., Sluyters-Rehbach, M. & Sluyters, J. H. The analysis of electrode impedances complicated by the presence of a constant phase element. *J. Electroanal. Chem. Interfacial Electrochem.* **176**, 275–295 (1984).
65. Orazem, M. E. & Tribollet, B. A tutorial on electrochemical impedance spectroscopy. *ChemTexts* **6**, 1–9 (2020).
66. Han, J., Chan, H. L., Wartenberg, M. G., Heinrich, H. H. & Scully, J. R. Distinguishing interfacial double layer and oxide-based capacitance on gold and pre-oxidized Fe-Cr in 1-ethyl-3-methylimidazolium methanesulfonate room temperature ionic liquid aqueous mixture. *Electrochem. Commun.* **122**, 106900 (2021).
67. Hamadou, L., Aïnouche, L., Kadri, A., Yahia, S. A. A. & Benbrahim, N. Electrochemical impedance spectroscopy study of thermally grown oxides exhibiting constant phase element behaviour. *Electrochim. Acta* **113**, 99–108 (2013).
68. Kelly, R. G., Scully, J. R., Shoesmith, D. & Buchheit, R. G. Electrochemical Techniques in Corrosion Science and Engineering, (CRC Press, 2002).
69. Lasia, A. Semiconductors and Mott-Schottky Plots. Electrochemical Impedance Spectroscopy and its Applications (Springer, 2014).
70. Ren, Y. & Zhou, G. Rediscovering Mott-Schottky plots: A knee-point in the plot for passive films on chromium. *J. Electrochem. Soc.* **164**, C182 (2017).
71. Moffat, T. P. & Latanision, R. M. An electrochemical and X-Ray photoelectron spectroscopy study of the passive state of chromium. *J. Electrochem. Soc.* **139**, 1869 (1992).
72. Haynes, W. M. CRC Handbook of Chemistry and Physics, 93rd Edition (CRC Press, 2012).
73. Hirschmann, E. et al. A new system for real-time data acquisition and pulse parameterization for digital positron annihilation lifetime spectrometers with high repetition rates. *J. Instrum.* **16**, P08001 (2021).
74. Birks, N., Meier, G. H., & Pettit, F. S. Introduction to the High-Temperature Oxidation of Metals, (Cambridge Univ. Press, 2009).
75. Desgranges, C., Lequien, F., Aublant, E., Nastar, M. & Monceau, D. Depletion and Voids Formation in the Substrate During High Temperature Oxidation of Ni–Cr Alloys. *Oxid. Met.* **79**, 93–105 (2013).
76. Poulain, C., Seyeux, A., Voyshnis, S. & Marcus, P. Volatilization and Transport Mechanisms During Cr Oxidation at 300 °C Studied In Situ by ToF-SIMS. *Oxid. Met.* **88**, 423–433 (2017).
77. Caplan, D. & Sproule, G. I. Discussion of "On High Temperature Oxidation of Chromium I. Oxidation of Annealed, Thermally Etched Chromium at 800°–1100 °C [K. P. Lillerud and P. Kofstad (pp. 2397–2410, Vol. 127, No. 11)]. *J. Electrochem. Soc.* **128**, 1388–1389 (1981).
78. Seyeux, A., Maurice, V. & Marcus, P. Oxide Film Growth Kinetics on Metals and Alloys. *J. Electrochem. Soc.* **160**, C189–C196 (2013).
79. Leistner, K., Toulemonde, C., Diawara, B., Seyeux, A. & Marcus, P. Oxide Film Growth Kinetics on Metals and Alloys. *J. Electrochem. Soc.* **160**, C197–C205 (2013).
80. Dignam, M. J. Transition layer model of the oxide–electrolyte interface. *Can. J. Chem.* **56**, 595–605 (1978).
81. Saeed, S. W. & Bjørheim, T. S. The Role of Space Charge at Metal/Oxide Interfaces in Proton Ceramic Electrochemical Cells. *J. Phys. Chem. C.* **124**, 20827–20833 (2020).
82. Malki, B., Le Bacq, O., Pasturel, A. & Baroux, B. Ab Initio Study of Water Related Defects in Cr_2O_3 and the Consequences for the Stability of Passive Films of Stainless Steels. *J. Electrochem. Soc.* **161**, C486–C493 (2014).
83. Liedke, M. O. et al. Open volume defects and magnetic phase transition in Fe 60 Al 40 transition metal aluminide. *J. Appl. Phys.* **117**, 163908 (2015).
84. Anwand, W., Brauer, G., Butterling, M., Kissener, H. R. & Wagner, A. Design and construction of a slow positron beam for solid and surface investigations. *Defect Diffus. Forum* **331**, 25–40 (2012).
85. Wagner, A. et al. Positron annihilation lifetime spectroscopy at a superconducting electron accelerator. *J. Phys. Conf. Ser.* **79**, 012004 (2017).
86. A. Wagner, M. Butterling, M.O. Liedke, K. Potzger, R. Krause-Rehberg, Positron annihilation lifetime and Doppler broadening spectroscopy at the ELBE facility. *AIP Conf. Proc*. 040003 (2018)
87. Qiu, J. et al. Electrical properties of thermal oxide scales on pure iron in liquid lead-bismuth eutectic. *Corros. Sci.* **176**, 109052 (2020).

ACKNOWLEDGEMENTS

This work was supported as part of FUTURE (Fundamental Understanding of Transport Under Reactor Extremes), an Energy Frontier Research Center funded by the U.S. Department of Energy, Office of Science, Basic Energy Sciences. Parts of this research were carried out at ELBE at the Helmholtz-Zentrum Dresden – Rossendorf e. V., a member of the Helmholtz Association. We would like to thank the facility staff for assistance. This work was partially supported by the Impulse-und Net-working fund of the Helmholtz Association (FKZ VH-VI-442 Memriox), and the Helmholtz Energy Materials Characterization Platform (03ET7015). This work was performed in part at the Analytical Instrumentation Facility (AIF) at North Carolina State University, which is supported by the State of North Carolina and the National Science Foundation (award number ECCS-1542015). This work made use of instrumentation at AIF acquired with support from the National Science Foundation (DMR-1726294). The AIF is a member of the North Carolina Research Triangle Nanotechnology Network (RTNN), a site in the National Nanotechnology Coordinated Infrastructure (NNCI).

AUTHOR CONTRIBUTIONS

R.A.—formal analysis, original draft preparation, editing, and revising the manuscript. H.L.C.—data collection, formal analysis, original draft preparation, and editing the manuscript. E.R.—data collection, formal analysis, original draft preparation, and editing the manuscript. J.Q.—data collection, formal analysis, and original draft preparation. R.S.—data collection, formal analysis, and original draft preparation. M.O.L.—data collection, formal analysis, and editing and revising the manuscript. M.B.—formal analysis and revising the manuscript. E.H.—data collection and revising the manuscript. A.G.A.—data collection and revising the manuscript. A.W.—data collection, funding acquisition and supervision. F.A.S.—editing and revising the manuscript. D.K.—supervision, editing, and revising the manuscript. B.P.U.—funding acquisition and revising the manuscript. P.H.—supervision, editing, and revising the manuscript. J.R.S.—supervision, editing, and revising the manuscript. All authors participated in the discussion of the results.

COMPETING INTERESTS

The authors declare no competing interests.

ADDITIONAL INFORMATION

Correspondence and requests for materials should be addressed to R. Auguste, H. L. Chan, P. Hosemann or J. R. Scully.